Systematics of nuclear charge distributions in the mass 60 region from elastic electron scattering and muonic x-ray measurements

H. D. Wohlfahrt,* O. Schwentker, G. Fricke, and H. G. Andresen
Institut für Kernphysik der Johannes Gutenberg-Universität, D-6500 Mainz, Germany

E. B. Shera
Los Alamos Scientific Laboratory, University of California, Los Alamos, New Mexico 87545
(Received 7 January 1980)

Precise ratios of elastic electron scattering cross sections for the nuclei ^{54,56,58}Fe, ^{58,60,62,64}Ni, and ^{64,66,68,70}Zn have been measured in the momentum-transfer region 0.6 fm^{-1} $\leq q \leq$ 2.3 fm^{-1}. The data were analyzed with a Fourier-Bessel parametrization of the charge distribution. Charge distribution differences were determined nearly model independently for the $\Delta A = 2$ isotope and isotone pairs. The $\Delta Z = 2$ isotone charge distribution differences show a strong shell effect, if one compares the Ni-Fe charge distribution differences, where the two added protons close the $1f_{7/2}$ shell, and the Zn-Ni charge distribution differences, where the two added protons start to fill the $2p_{3/2}$ shell. For the $\Delta N = 2$ isotopes we observe a nearly constant increase of the "half density radius" in the investigated region of the $2p_{3/2}$, $1f_{5/2}$, and $2p_{1/2}$ neutron shells. However, the skin thickness of the charge distribution increases strongly at the beginning (^{56}Fe-^{54}Fe) and decreases at the end (^{70}Zn-^{68}Zn) of these shells by adding two neutrons. The rms radii differences deduced from a combined analysis of the electron scattering data and present muonic x-ray data show the same trend. These differences, determined model independently with a typical accuracy of some 10^{-3} fm, decrease nearly linearly with increasing neutron number in the investigated region $28 \leq N \leq 40$. These isotope shifts are nearly independent of the proton configuration of the involved nuclei, which indicates that the added neutrons interact primarily with the proton core rather than with the valence protons. Recent calculations, which include ground state correlations, show that the observed isotope shifts reflect deformation changes caused by changes of the amplitude of the zero-point quadrupole surface oscillations. A comparison of the experimental charge distribution differences with results of density dependent Hartree-Fock calculations also indicates the importance of deformation changes. The core rearrangement due to added protons, deduced from the measured isotone charge distribution differences, and the core rearrangements due to added neutrons, directly measured by the isotope shifts, are similar. The last two nucleons of both the $1f_{7/2}$ neutron and proton shell cause core polarizations, resulting in a smaller charge core radius.

[NUCLEAR STRUCTURE ^{54,56,58}Fe, ^{58,60,62,64}Ni, and ^{64,66,68,70}Zn; elastic electron scattering differential cross sections $d\sigma/d\Omega(E,\theta)$ and ratios at E=100, 150, 275 MeV; model-independent charge distribution differences for isotones and isotopes; model-independent radial moments $\langle r^k \rangle^{1/k}$ and $\Delta \langle r^k \rangle^{1/k}$, deduced from a combined elastic electron and muonic x-ray data analysis; charge distribution differences, compared with Hartree-Fock calculations, and calculations considering ground state correlations.]

I. INTRODUCTION

The investigation of nuclear ground state charge distributions of isotopes provides detailed information about the rearrangement of the nuclear charge distribution in response to the addition of neutrons. The charge distribution of neighboring isotones depends predominantly on the spatial distributions of the added protons and to a minor extent on the rearrangement of the proton core due to the added protons.

It is well known that smooth interpolations of the dependence of charge distribution parameters on the nucleon number A,[1-4] as expressed by the following relationship for the ground state root mean square (rms) equivalent radius[2]

$$R = 1.120A^{1/3} + 2.009A^{-1/3} - 1.513A^{-1},$$

represent only approximations which must be modified by nuclear shell structure and deformation effects. This has already been demonstrated by several measurements of improved accuracy.[5-8]

The goal of this experiment was the investigation of systematic shell structure effects by means of accurately measured ground state charge distribution differences of nuclei in the vicinity of the magic proton number 28. The nuclear chart, shown in Fig. 1, displays in a Z versus N plot all nuclei and their relevant shell model configurations, whose elastic cross section ratios have been precisely measured with the electron scattering

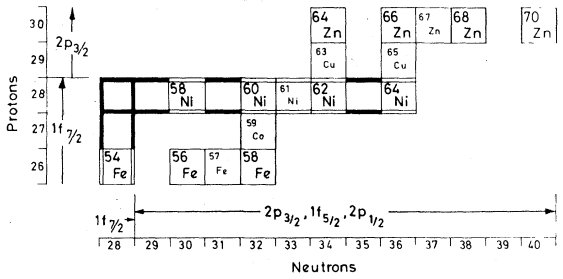

FIG. 1. Nuclei investigated and associated shell model configuration.

facility of the Mainz 300 MeV linac. This paper presents only the results for the even A nuclei: ^{54,56,58}Fe, ^{58,60,62,64}Ni, and ^{64,66,68,70}Zn. The results for the odd A nuclei ^{59}Co and ^{63,65}Cu (Ref. 9) will be presented in a subsequent paper.

In a Los Alamos Scientific Laboratory (LASL)–Mainz collaboration,[8] precise measurements of the $2p_{3/2}$-$1s_{1/2}$ and $2p_{1/2}$-$1s_{1/2}$ muonic atom x-ray transitions have been performed for all nuclei depicted in Fig. 1 (except ^{67}Zn), at the Los Alamos Meson Physics Facility (LAMPF) stopped muon channel. The information about nuclear charge distributions, which can be obtained from a separate and a combined analysis of these two data sets, can be characterized as follows.

Electron scattering data essentially determine the Fourier transform of the nuclear charge distribution $\rho(r)$ even in the framework of a phase shift analysis. Therefore these measurements determine directly the charge distribution and charge distribution differences, provided the measurements are accurate enough and extend over a sufficiently large range of momentum transfer. By using a Fourier-Bessel expansion technique,[10] realistic error bands can be derived for the charge distributions and their differences, which reflect both the statistical error and the error due to the limited range of measured momentum transfer.

Muonic data, on the other hand, determine integral quantities. Within the limits of present experimental errors the muonic transition energies determine certain Barrett radial moments $\langle r^k e^{-\alpha r}\rangle$ of the nuclear charge distribution.[11] For the nuclei under consideration ($Z \simeq 28$), the $2p-1s$ transitions of the muonic atoms provide precise values for the Barrett moments with $k \simeq 2.12$ and $\alpha \simeq 0.076$ fm^{-1}.

The main contribution to the charge distribution error band of a properly devised electron scattering experiment should be associated with the unmeasured momentum transfer range. In this case a combined analysis of electron scattering data and muonic atom transition energies will only insignificantly improve the charge distribution error band. However, it greatly reduces the errors of the model-independent radial moments $\langle r^k\rangle^{1/k}$ ($1 \leq k \leq 4$). This improvement is not only restricted to the model-independent determination of the rms radius, which is the moment most closely related to the precisely measured Barrett moment, but extends to lower and higher radial moments. This will be discussed later in more detail.

II. ELASTIC ELECTRON SCATTERING

A. Experimental arrangement

The experiment was performed at the electron scattering facility at the Mainz 300 MeV linear accelerator. Since the facility has already been described elsewhere,[12] the discussion of the experimental details will be restricted to those points that are specifically relevant to the present experiment.

After the installation of an energy compressing system[13] between the accelerator and the beam handling system, an average current of up to 20 μA with a momentum spread of 0.1% was available at the target. With this high beam intensity, spectra at large momentum transfer could be measured with good statistical accuracy. Beam position monitors in front of the energy defining system and in front of the target were used to provide both momentum stability and stability of the beam position at the target. The beam current was measured with an accuracy of $\leq$0.5% by a ferrite monitor designed by Stephan.[14,15] A second spectrometer, installed at a fixed scattering angle of 28 degrees, monitored the product beam current times target thickness during the experiment. Changes of the effective target thickness caused by beam position changes and the inhomogeneity of the targets could be observed and corrected.[16] This spectrometer was also used to determine relative target thicknesses by electron scattering at low momentum transfer.

For the measurement of accurate cross section ratios, up to seven targets were mounted on a stepwise rotating wheel, and each target was measured repeatedly for intervals of, typically, ten seconds.[17] Since the targets were measured quasi-simultaneously, the influence of instabilities of the apparatus on the measured cross section ratios was minimized. The accuracy of the measured cross section ratios was thus determined only by the uncertainty of the relative target thicknesses and the target impurities.

B. Targets

The target foils, which had dimensions of 1.5 $\times$ 5.0 cm^2, consisted of highly enriched isotopes.[18]

TABLE I. Isotopic compositions of the targets. The quoted target thicknesses have been determined relative to ^{12}C with an accuracy of ±0.5%. The relative accuracy of the target thicknesses of the investigated nuclei is ±0.3%.

Target	Isotopic abundance atomic %					Contamination %	Thickness (mg/cm^2)
	^{12}C	^{13}C					
^{12}C	98.89	1.11					85.0
	^{54}Fe	^{56}Fe	^{57}Fe	^{58}Fe			
^{54}Fe	97.12	2.88	<0.10	<0.10		<0.20	98.3
^{56}Fe	0.03	99.93	0.03	<0.02		<0.20	99.9
^{58}Fe	0.46	15.57	1.48	82.48		3 ± 1 (Ref. 20)	42.6
	^{58}Ni	^{60}Ni	^{61}Ni	^{62}Ni	^{64}Ni		
^{58}Ni	99.95	0.05	<0.02	<0.02	<0.02	<0.15	95.2
^{60}Ni	0.21	99.79	<0.05	<0.05	<0.05	<2.00 (Ref. 19)	98.7
^{62}Ni	0.46	0.81	<0.03	98.70	<0.01	<0.10	99.0
^{64}Ni	0.92	0.73	0.05	0.38	97.92	<0.20	99.0
	^{64}Zn	^{66}Zn	^{67}Zn	^{68}Zn	^{70}Zn		
^{64}Zn	99.66	0.21	<0.02	0.09	<0.02	<0.05	92.7
^{66}Zn	1.20	97.80	0.40	0.60	<0.05	2.7 ± 0.2 (Ref. 20)	99.5
^{68}Zn	0.80	0.46	0.16	98.50	<0.05	<0.10	94.7
^{70}Zn	12.73	8.05	2.32	9.44	67.56	<0.05	21.3

Since electron scattering experiments revealed in some targets the existence of other elements by their recoil shifted elastic lines, target impurities were reexamined by mass spectroscopy,[19] slow neutron activation, and γ-fluorescence[20] measurements. The isotopic purities, the contaminations, and the thicknesses of the targets are listed in Table I.

Relative target thicknesses can be determined with good precision by means of electron scattering at low momentum transfer, using the fixed angle spectrometer of the Mainz electron scattering facility.[16] This method is based on the fact that electron scattering cross sections depend, in the limit of low momentum transfer, only insignificantly on the specific charge distribution, so that the ratio of the counting rates for various targets depends predominantly on the relative target thicknesses.

Relative target thicknesses were determined by using the following iterative procedure. Starting with values for the average target thickness, defined by the weight per area ratio, charge distributions were derived from all measured electron scattering data. These charge distributions were then used to extrapolate the expected counting rate ratios for the fixed angle spectrometer measurement at $q = 0.25$ fm^{-1}. For this small q value the difference between the actual measurement and the extrapolated value can in good approximation be attributed to the inexact starting value for the target thickness. After applying this correction factor, the procedure is repeated and converges after two to four iterations.

The model dependence of this method is mainly caused by the influence of the rms radius on the low q cross section. It is quite obvious that the model-dependent error is considerably reduced for relative measurements between neighboring nuclei. In this case the relative target thicknesses can be determined with an error of ±0.3%. If absolute cross sections are determined (see Sec. II C) by measuring relative to the absolutely known ^{12}C cross section, the model-dependent error of this method becomes larger and has to be appropriately considered. In order to check the procedure described above, the relative target thicknesses were also determined by means of monochromatic x-ray absorption.[21] The results of both methods agreed within their respective errors of ±0.5%.

C. Cross sections

The measurements were performed at energies of 100, 150, and 275 MeV and scattering angles from 56 to 110 degrees, which corresponds to an effective momentum transfer from 0.6 to 2.3 fm^{-1}.

TABLE II. Experimental differential cross section ratios as a function of the energies and angles of the scattered electrons. The cross section ratios are corrected for the finite solid angle of the spectrometer, multiple scattering in the target, and radiation losses. Only statistical errors are quoted.

E (MeV)	θ (deg)	Cross section ratio $^{54}Fe/^{60}Ni$	$^{56}Fe/^{60}Ni$	$^{58}Fe/^{60}Ni$
100.0	60.0	0.960 ± 0.008	0.918 ± 0.008	0.875 ± 0.008
	65.0	0.987 ± 0.008	0.927 ± 0.008	0.891 ± 0.008
	70.0	1.011 ± 0.008	0.947 ± 0.008	0.895 ± 0.009
	75.0	1.008 ± 0.009	0.970 ± 0.008	0.909 ± 0.009
	80.0	1.050 ± 0.008	0.986 ± 0.008	0.907 ± 0.009
	85.0	1.084 ± 0.009	1.006 ± 0.008	0.941 ± 0.009
	90.0	1.136 ± 0.011	1.041 ± 0.010	0.950 ± 0.009
	95.0	1.174 ± 0.013	1.055 ± 0.012	0.984 ± 0.009
	100.0	1.215 ± 0.015	1.094 ± 0.014	0.988 ± 0.010
	105.0	1.234 ± 0.012	1.112 ± 0.011	1.003 ± 0.010
	110.0	1.222 ± 0.014	1.098 ± 0.014	0.979 ± 0.010
150.0	65.0	1.184 ± 0.014	1.078 ± 0.013	0.935 ± 0.011
	67.5	1.203 ± 0.012	1.083 ± 0.011	0.954 ± 0.010
	70.0	1.203 ± 0.013	1.078 ± 0.012	0.932 ± 0.010
	72.5	1.147 ± 0.012	1.013 ± 0.011	0.906 ± 0.010
	75.0	1.022 ± 0.012	0.908 ± 0.011	0.847 ± 0.010
	77.5	0.867 ± 0.009	0.781 ± 0.008	0.767 ± 0.009
	80.0	0.750 ± 0.009	0.691 ± 0.008	0.691 ± 0.009
	82.5	0.657 ± 0.007	0.630 ± 0.007	0.671 ± 0.009
	85.0	0.642 ± 0.005	0.632 ± 0.005	0.665 ± 0.009
	87.5	0.658 ± 0.008	0.651 ± 0.008	0.658 ± 0.009
	90.0	0.674 ± 0.006	0.655 ± 0.006	0.673 ± 0.008
	92.5	0.732 ± 0.010	0.704 ± 0.009	0.692 ± 0.009
	95.0	0.728 ± 0.010	0.693 ± 0.010	0.701 ± 0.009
	97.5	0.766 ± 0.011	0.738 ± 0.010	0.707 ± 0.008
	100.0	0.814 ± 0.013	0.774 ± 0.012	0.709 ± 0.009
	105.0	0.894 ± 0.015	0.826 ± 0.015	0.755 ± 0.009
	110.0	0.959 ± 0.019	0.836 ± 0.017	0.765 ± 0.009
275.0	56.0	0.984 ± 0.011	0.882 ± 0.010	0.816 ± 0.011
	58.0	1.060 ± 0.012	0.914 ± 0.011	0.841 ± 0.011
	60.0	1.104 ± 0.013	0.954 ± 0.010	0.867 ± 0.011
	62.0	1.228 ± 0.009	1.026 ± 0.007	0.891 ± 0.011
	64.0	1.314 ± 0.013	1.066 ± 0.011	0.905 ± 0.014
	66.0	1.501 ± 0.019	1.183 ± 0.016	0.959 ± 0.012
	68.0	1.625 ± 0.023	1.240 ± 0.019	1.019 ± 0.013
	70.0	1.877 ± 0.034	1.404 ± 0.027	1.035 ± 0.011
	72.0	2.185 ± 0.042	1.515 ± 0.032	1.046 ± 0.023
	74.0	2.191 ± 0.064	1.490 ± 0.041	1.045 ± 0.033
	76.0	1.588 ± 0.028	1.160 ± 0.022	0.825 ± 0.034
	78.0	0.848 ± 0.033	0.606 ± 0.026	0.570 ± 0.026
	80.0	0.475 ± 0.019	0.430 ± 0.018	0.515 ± 0.023
	82.0	0.472 ± 0.021	0.423 ± 0.020	0.544 ± 0.022
	84.0	0.534 ± 0.018	0.529 ± 0.018	0.618 ± 0.023
	86.0	0.630 ± 0.021	0.585 ± 0.020	0.611 ± 0.022
	88.0	0.753 ± 0.029	0.631 ± 0.025	0.672 ± 0.027
	90.0	0.783 ± 0.024	0.695 ± 0.022	0.660 ± 0.029
	92.0	0.941 ± 0.036	0.732 ± 0.030	0.674 ± 0.030
	96.0	1.074 ± 0.044	0.851 ± 0.037	0.751 ± 0.041
	98.0	1.198 ± 0.065	0.840 ± 0.050	0.776 ± 0.048
	102.0	1.188 ± 0.075	0.943 ± 0.063	0.663 ± 0.070
	106.0	1.493 ± 0.101	0.991 ± 0.076	0.979 ± 0.119

TABLE II. (*Continued.*)

E (MeV)	θ (deg)	Cross section ratio $^{60}Ni/^{12}C$	$^{58}Ni/^{60}Ni$	$^{62}Ni/^{60}Ni$	$^{64}Ni/^{60}Ni$
100.0	60.0	9.198 ± 0.066	1.026 ± 0.009	0.957 ± 0.009	0.962 ± 0.008
	65.0	7.752 ± 0.056	1.035 ± 0.009	0.955 ± 0.008	0.953 ± 0.009
	70.0	6.360 ± 0.054	1.048 ± 0.008	0.958 ± 0.008	0.938 ± 0.009
	75.0	5.115 ± 0.037	1.060 ± 0.009	0.943 ± 0.008	0.923 ± 0.009
	80.0	4.016 ± 0.035	1.078 ± 0.008	0.957 ± 0.008	0.896 ± 0.008
	85.0	3.038 ± 0.025	1.083 ± 0.009	0.928 ± 0.008	0.897 ± 0.008
	90.0	2.325 ± 0.019	1.093 ± 0.011	0.947 ± 0.010	0.872 ± 0.008
	95.0	1.678 ± 0.013	1.099 ± 0.013	0.911 ± 0.011	0.853 ± 0.009
	100.0	1.225 ± 0.010	1.091 ± 0.014	0.902 ± 0.012	0.814 ± 0.009
	105.0	0.871 ± 0.007	1.100 ± 0.011	0.891 ± 0.009	0.799 ± 0.009
	110.0	0.631 ± 0.005	1.091 ± 0.018	0.890 ± 0.011	0.806 ± 0.010
150.0	65.0	1.087 ± 0.010	1.099 ± 0.013	0.906 ± 0.011	0.824 ± 0.009
	67.5	0.794 ± 0.006	1.085 ± 0.011	0.894 ± 0.010	0.804 ± 0.009
	70.0	0.588 ± 0.006	1.069 ± 0.012	0.881 ± 0.010	0.804 ± 0.009
	72.5	0.451 ± 0.004	1.072 ± 0.011	0.884 ± 0.010	0.838 ± 0.008
	75.0	0.380 ± 0.003	1.053 ± 0.013	0.924 ± 0.012	0.907 ± 0.009
	77.5	0.367 ± 0.003	0.987 ± 0.011	0.959 ± 0.010	0.981 ± 0.009
	80.0	0.415 ± 0.004	0.993 ± 0.011	1.023 ± 0.012	1.068 ± 0.011
	82.5	0.488 ± 0.004	0.957 ± 0.010	1.031 ± 0.012	1.101 ± 0.012
	85.0	0.590 ± 0.006	0.958 ± 0.008	1.022 ± 0.008	1.124 ± 0.008
	87.5	0.757 ± 0.007	0.962 ± 0.012	1.041 ± 0.013	1.112 ± 0.011
	90.0	0.910 ± 0.009	0.966 ± 0.009	1.022 ± 0.010	1.099 ± 0.010
	92.5	1.081 ± 0.009	0.999 ± 0.013	1.015 ± 0.014	1.087 ± 0.011
	95.0	1.246 ± 0.013	0.981 ± 0.015	1.005 ± 0.015	1.072 ± 0.010
	97.5	1.446 ± 0.012	0.993 ± 0.014	0.992 ± 0.014	1.053 ± 0.011
	100.0	1.627 ± 0.015	1.015 ± 0.016	0.980 ± 0.015	1.050 ± 0.010
	105.0	1.887 ± 0.018	1.048 ± 0.018	0.968 ± 0.017	1.025 ± 0.013
	110.0	2.126 ± 0.021	1.076 ± 0.022	0.941 ± 0.020	0.975 ± 0.015
275.0	56.0	2.288 ± 0.029	1.089 ± 0.012	0.912 ± 0.010	0.968 ± 0.012
	58.0	2.544 ± 0.033	1.091 ± 0.013	0.904 ± 0.011	0.912 ± 0.011
	60.0	2.699 ± 0.027	1.147 ± 0.012	0.908 ± 0.010	0.888 ± 0.012
	62.0	2.766 ± 0.026	1.187 ± 0.008	0.886 ± 0.006	0.848 ± 0.009
	64.0	2.761 ± 0.031	1.200 ± 0.013	0.867 ± 0.010	0.784 ± 0.010
	66.0	2.611 ± 0.024	1.286 ± 0.017	0.849 ± 0.013	0.736 ± 0.007
	68.0	2.359 ± 0.023	1.265 ± 0.019	0.769 ± 0.013	0.676 ± 0.010
	70.0	2.133 ± 0.027	1.404 ± 0.027	0.760 ± 0.017	0.621 ± 0.011
	72.0	1.880 ± 0.032	1.430 ± 0.026	0.716 ± 0.016	0.570 ± 0.015
	74.0	1.710 ± 0.041	1.322 ± 0.038	0.753 ± 0.022	0.744 ± 0.023
	76.0	2.276 ± 0.066	1.167 ± 0.023	0.960 ± 0.019	1.106 ± 0.035
	78.0	5.945 ± 0.193	0.895 ± 0.037	1.193 ± 0.046	1.581 ± 0.062
	80.0	18.367 ± 0.568	0.775 ± 0.027	1.063 ± 0.034	1.545 ± 0.047
	82.0	32.888 ± 0.960	0.901 ± 0.041	1.119 ± 0.051	1.405 ± 0.044
	84.0	24.353 ± 0.706	0.947 ± 0.030	1.087 ± 0.033	1.337 ± 0.035
	86.0	16.192 ± 0.463	1.028 ± 0.033	1.083 ± 0.035	1.215 ± 0.035
	88.0	10.816 ± 0.485	0.955 ± 0.039	1.011 ± 0.040	1.192 ± 0.033
	90.0	8.361 ± 0.353	1.062 ± 0.033	0.983 ± 0.032	1.080 ± 0.045
	92.0	6.291 ± 0.245	1.096 ± 0.043	0.977 ± 0.040	1.072 ± 0.033
	96.0	3.931 ± 0.170	1.132 ± 0.047	0.942 ± 0.041	0.888 ± 0.039
	98.0	3.062 ± 0.141	1.146 ± 0.064	0.861 ± 0.053	0.867 ± 0.054
	102.0	1.800 ± 0.119	1.120 ± 0.073	0.818 ± 0.058	0.813 ± 0.049
	106.0	1.192 ± 0.096	1.216 ± 0.087	0.813 ± 0.057	0.707 ± 0.086

TABLE II. (*Continued.*)

E (MeV)	θ (deg)	Cross section ratio $^{64}Zn/^{60}Ni$	$^{66}Zn/^{60}Ni$	$^{68}Zn/^{60}Ni$	$^{70}Zn/^{60}Ni$
100.0	60.0	1.048 ± 0.009	1.026 ± 0.009	0.997 ± 0.009	0.967 ± 0.011
	65.0	1.030 ± 0.010	1.007 ± 0.010	0.960 ± 0.010	0.928 ± 0.012
	70.0	0.991 ± 0.009	0.984 ± 0.009	0.938 ± 0.009	0.887 ± 0.011
	75.0	0.971 ± 0.009	0.959 ± 0.009	0.911 ± 0.009	0.867 ± 0.011
	80.0	0.927 ± 0.009	0.906 ± 0.008	0.868 ± 0.008	0.808 ± 0.010
	85.0	0.911 ± 0.009	0.888 ± 0.008	0.821 ± 0.008	0.777 ± 0.010
	90.0	0.893 ± 0.008	0.860 ± 0.008	0.791 ± 0.008	0.721 ± 0.009
	95.0	0.864 ± 0.009	0.836 ± 0.009	0.758 ± 0.009	0.691 ± 0.010
	100.0	0.833 ± 0.009	0.805 ± 0.009	0.711 ± 0.008	0.658 ± 0.009
	105.0	0.821 ± 0.009	0.810 ± 0.009	0.706 ± 0.008	0.646 ± 0.009
	110.0	0.841 ± 0.010	0.838 ± 0.010	0.740 ± 0.009	0.683 ± 0.010
150.0	65.0	0.885 ± 0.010	0.829 ± 0.010	0.733 ± 0.009	0.664 ± 0.011
	67.5	0.852 ± 0.010	0.823 ± 0.010	0.737 ± 0.009	0.664 ± 0.011
	70.0	0.882 ± 0.010	0.853 ± 0.009	0.775 ± 0.009	0.707 ± 0.011
	72.5	0.979 ± 0.009	0.959 ± 0.009	0.894 ± 0.008	0.879 ± 0.011
	75.0	1.075 ± 0.011	1.055 ± 0.010	1.071 ± 0.011	1.053 ± 0.014
	77.5	1.190 ± 0.010	1.182 ± 0.010	1.246 ± 0.011	1.261 ± 0.014
	80.0	1.242 ± 0.012	1.258 ± 0.012	1.343 ± 0.013	1.383 ± 0.017
	82.5	1.240 ± 0.013	1.279 ± 0.014	1.361 ± 0.015	1.445 ± 0.018
	85.0	1.228 ± 0.008	1.261 ± 0.008	1.364 ± 0.009	1.398 ± 0.012
	87.5	1.175 ± 0.012	1.207 ± 0.012	1.304 ± 0.013	1.360 ± 0.016
	90.0	1.133 ± 0.010	1.148 ± 0.010	1.238 ± 0.011	1.256 ± 0.014
	92.5	1.130 ± 0.011	1.112 ± 0.011	1.190 ± 0.012	1.240 ± 0.015
	95.0	1.068 ± 0.010	1.063 ± 0.010	1.112 ± 0.010	1.128 ± 0.014
	97.5	1.028 ± 0.011	1.028 ± 0.011	1.067 ± 0.011	1.080 ± 0.014
	100.0	0.996 ± 0.010	0.991 ± 0.010	1.028 ± 0.010	1.040 ± 0.013
	105.0	0.941 ± 0.013	0.938 ± 0.012	0.944 ± 0.013	0.956 ± 0.015
	110.0	0.869 ± 0.014	0.868 ± 0.014	0.847 ± 0.014	0.871 ± 0.017
275.0	56.0	0.845 ± 0.010	0.838 ± 0.010	0.838 ± 0.010	0.822 ± 0.013
	58.0	0.790 ± 0.010	0.778 ± 0.010	0.758 ± 0.010	0.768 ± 0.013
	60.0	0.762 ± 0.010	0.724 ± 0.009	0.678 ± 0.009	0.645 ± 0.012
	62.0	0.710 ± 0.008	0.664 ± 0.008	0.612 ± 0.007	0.593 ± 0.010
	64.0	0.658 ± 0.009	0.599 ± 0.008	0.511 ± 0.007	0.492 ± 0.010
	66.0	0.605 ± 0.006	0.542 ± 0.006	0.444 ± 0.005	0.403 ± 0.007
	68.0	0.540 ± 0.009	0.476 ± 0.008	0.365 ± 0.006	0.323 ± 0.009
	70.0	0.521 ± 0.010	0.459 ± 0.009	0.326 ± 0.008	0.326 ± 0.012
	72.0	0.516 ± 0.014	0.533 ± 0.014	0.422 ± 0.012	0.437 ± 0.018
	74.0	0.687 ± 0.022	0.787 ± 0.025	0.906 ± 0.028	0.989 ± 0.039
	76.0	1.062 ± 0.035	1.250 ± 0.038	1.554 ± 0.046	1.968 ± 0.069
	78.0	1.334 ± 0.055	1.637 ± 0.064	2.155 ± 0.082	2.476 ± 0.110
	80.0	1.144 ± 0.038	1.391 ± 0.042	1.734 ± 0.053	1.885 ± 0.071
	82.0	1.066 ± 0.037	1.280 ± 0.041	1.531 ± 0.048	1.602 ± 0.069
	84.0	0.971 ± 0.028	1.034 ± 0.029	1.222 ± 0.034	1.269 ± 0.048
	86.0	0.847 ± 0.027	0.925 ± 0.029	1.030 ± 0.031	1.105 ± 0.045
	88.0	0.800 ± 0.026	0.812 ± 0.026	0.870 ± 0.028	0.900 ± 0.040
	90.0	0.685 ± 0.033	0.686 ± 0.033	0.735 ± 0.036	0.681 ± 0.052
	92.0	0.696 ± 0.025	0.652 ± 0.024	0.666 ± 0.025	0.706 ± 0.042
	96.0	0.569 ± 0.030	0.436 ± 0.026	0.474 ± 0.028	0.459 ± 0.047
	98.0	0.383 ± 0.036	0.450 ± 0.038	0.466 ± 0.039	0.444 ± 0.072
	102.0	0.412 ± 0.039	0.339 ± 0.039	0.396 ± 0.038	0.385 ± 0.369
	106.0	0.220 ± 0.246	0.193 ± 0.271	0.231 ± 0.289	0.218 ± 1.315

The cross sections of the twelve investigated nuclei were determined with three different target combinations: (^{58}Fe, ^{60}Ni, ^{12}C); (^{54,56}Fe, ^{58,60,62}Ni); (^{60,64}Ni, ^{64,66,68,70}Zn). For each run the ^{60}Ni target served as a reference.

The cross sections of ^{60}Ni were determined relative to ^{12}C using the absolute ^{12}C cross sections recently measured by Reuter *et al.*[22] All other cross sections were measured relative to ^{60}Ni. The cross section ratios are presented in Table II. All of these data, which were obtained in several experimental runs, have been slightly corrected to refer exactly to energies of 100.0, 150.0, and 275.0 MeV respectively. The correction factor was obtained from charge distributions fitting the original data. The cross section data were derived by applying radiative corrections using the formulae for the Schwinger, bremsstrahlung, and Landau straggling corrections, given by Maximon,[23] and Isabell and Bishop,[24] using a cutoff energy of 0.5 MeV. For the 100 MeV data of ^{58}Fe a cutoff energy of 0.2 MeV was chosen in order to avoid corrections for the Si contamination. For all nuclei small corrections for the isotopic impurities and the contaminations listed in Table I have been applied. The influence of the finite solid angle acceptance of the spectrometer and the multiple scattering in the target was considered by using the procedure described by Lyman *et al.*[25]

The errors listed in Table II consider only the counting statistics, since systematic errors cancel for the cross section ratios which are used to determine charge distribution differences. This statement is not correct, however, if target impurities are present. In the case of ^{66}Zn such target impurities were the dominant error. They cause an uncertainty in the cross section of 2%. The calibration errors of the energy and angle are 0.1% and 0.04 degree respectively.

Figure 2 displays cross section ratios for two isotone and isotope pairs as a function of the effective momentum transfer. For both the isotone pairs ^{64}Zn, ^{62}Ni and ^{58}Ni, ^{56}Fe and the isotope pairs ^{56,54}Fe and ^{64,62}Ni, the measured cross section ratios are significantly different. This fact will be discussed in more detail in Sec. II E.

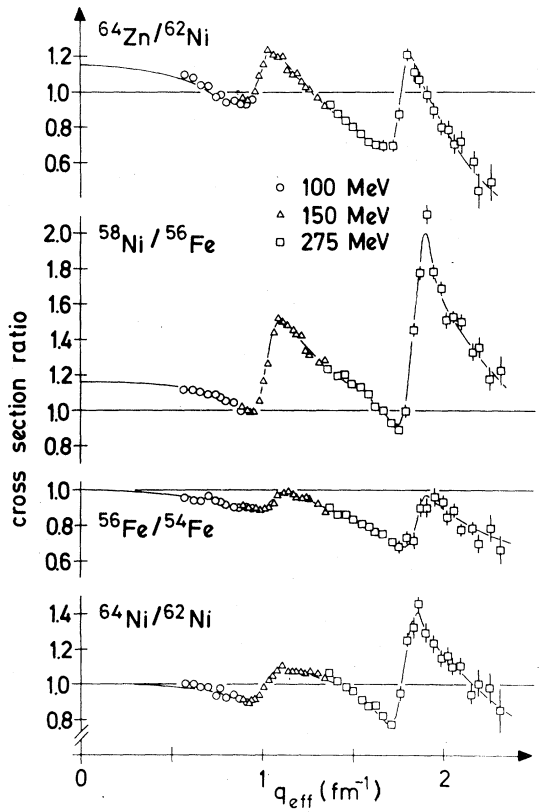

FIG. 2. Experimental cross section ratios as a function of the effective momentum transfer for selected isotone and isotope pairs. The curves are best fits to the data using Fourier-Bessel parametrized charge distribution differences.

D. Analysis of the cross sections

A first analysis of the data was performed using "parabolic modified Gaussian" charge distributions[5] to fit the measured cross sections. The resulting χ^2 per degree of freedom was about 2.6 for all nuclei. This relatively large value is mainly caused by systematic deviations between measured and fitted cross sections in the diffraction minima and at high momentum transfers, which indicates clearly the deficiency of this charge distribution model. In addition, the use of insufficiently flexible charge distribution models, whose parameters are not directly related to measured quantities, may underestimate the charge distribution error band in regions of the charge distribution that are insensitive to the measured momentum transfer range.

To avoid these problems several methods have been developed[10,26-28] to obtain a more realistic charge distribution. In the analysis of our data we used the Fourier-Bessel expansion of the charge distribution introduced by Dreher *et al.*[10]:

$$\rho(r) = \begin{cases} (Ze/4\pi) \sum_{\nu} a_\nu j_0(q_\nu r), & r \le R_{\max} \\ 0, & r > R_{\max}. \end{cases} \quad (1)$$

$R_{\max}$ is the cutoff radius of the charge distribution.

In the framework of a plane wave approximation, the parameters a_ν are connected with the form factor values at the momentum transfer $q_\nu = \pi\nu/R_{max}$:

$$a_\nu = 2(\pi\nu)^2/R_{max}{}^3 F(q_\nu) . \quad (2)$$

This charge distribution parametrization has the advantage that the first N coefficients a_ν and their errors δa_ν are directly related to measured quantities, where $N = [q_{max} \times R_{max}/\pi]$ is given by the maximum momentum transfer q_{max}.

The influence of the unmeasured parameters a_ν on the charge distribution error band can be determined by using the upper bound estimate[10] for the high momentum transfer asymptotic behavior of the form factor:

$$|F(q_\nu)| \leq C q_\nu^{-4} F_p(q_\nu), \quad q_\nu > q_{max} \quad (3)$$

where $F_p(q_\nu)$ represents the proton form factor. The constant C can be determined by matching the asymptotic behavior to the last measured cross section maximum. The validity of this procedure is checked in Fig. 3 by comparing our assumptions with the ^{58}Ni data, measured at Saclay[26] for high momentum transfer.

The matching of the asymptotic behavior of the form factor and the choice of the cutoff radius R_{max} beyond which $\rho(r)$ is assumed to be zero are the only model assumptions used in this method.

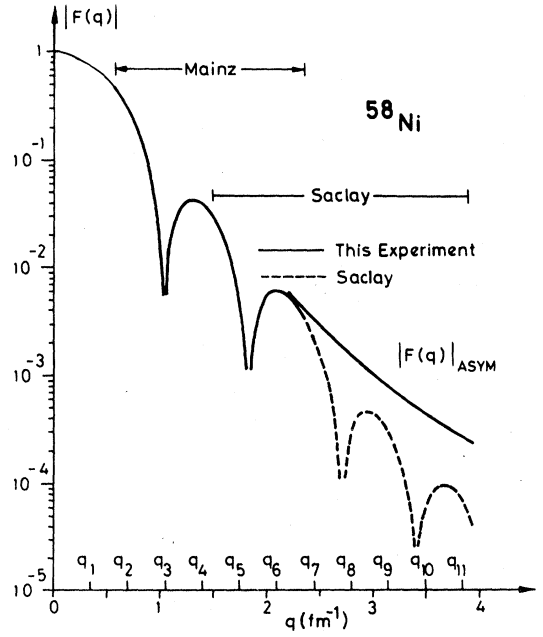

FIG. 3. Illustration of the Fourier-Bessel method, showing the positions q_ν for a cutoff radius $R_{max} = 9$ fm. Comparison of the upper bound for the asymptotic form factor $|F(q)|_{ASYM}$ estimated from this experiment ($q_{max} = 2.3$ fm^{-1}) with the form factors measured at Saclay by Sick *et al.* (Ref. 26) ($q_{max} = 4$ fm^{-1}).

Because of the linear relationship between $\rho(r)$ and $F(q)$, the form factor difference between two nuclei can be used to derive the charge distribution difference and its associated error band. The Fourier-Bessel expansion parameters a_ν and their errors were actually determined by a fit to the measured cross sections by means of a phase shift analysis. The model-dependent contribution to the error band of the charge distribution can still be determined according to the above method.

Since the charge distribution difference $\Delta\rho_{AB} = \rho_A - \rho_B$ between two nuclei is uniquely specified by the cross section ratio $[(d\sigma/d\Omega)_A/(d\sigma/d\Omega)_B]^{exp}$, we exploited the high experimental accuracy of this ratio to minimize the uncertainty of the charge distribution differences. By fitting the coefficients $a_\nu(A)$ for the charge distribution of the nucleus A to the quantity $[(d\sigma/d\Omega)_A/(d\sigma/d\Omega)_B]^{exp}[d\sigma/d\Omega]_B^{fit}$, where $(d\sigma/d\Omega)_B^{fit}$ are the cross sections for the best fit parameters $a_\nu(B)$ of the nucleus B, the errors of the Fourier-Bessel expansion parameter differences $\Delta a_\nu = a_\nu(A) - a_\nu(B)$ are determined by the relatively small uncertainty of the measured cross section ratio.

E. Results

Charge distribution differences $\Delta\rho(r)$, derived with the Fourier-Bessel expansion techniques described in Sec. IID, are shown in Fig. 4. The error bands, depicted by solid lines, refer to the results of a combined analysis of electron scattering and muonic atom data, which will be discussed in Sec. III. This error band includes the statistical errors of the measured cross section ratios as well as the uncertainty of the cross section ratios for nonmeasured high momentum transfers being limited by the upper bound given by Eq. (3). Charge distribution differences measured relative to ^{66}Zn have not been plotted, since the uncertainties due to the iron contaminations resulted in error bands that are quite large.

Charge distribution differences for isotope pairs, as shown in Fig. 4, can be described by core polarization effects. The charge which is moved from the inner region to the outer region of the nucleus corresponds to 40% of one proton charge at the beginning of the $2p_{3/2}$ neutron shell and decreases with increasing neutron number. It is nearly independent of the proton number (see Fig. 9). Although the plotted charge distribution differences already display the core polarization in full detail, two characteristic shape parameters have been introduced to emphasize the general trend of the polarization: the half "central charge density" radius c_{FB}, defined as the radius at which the Fourier-Bessel charge distribution has

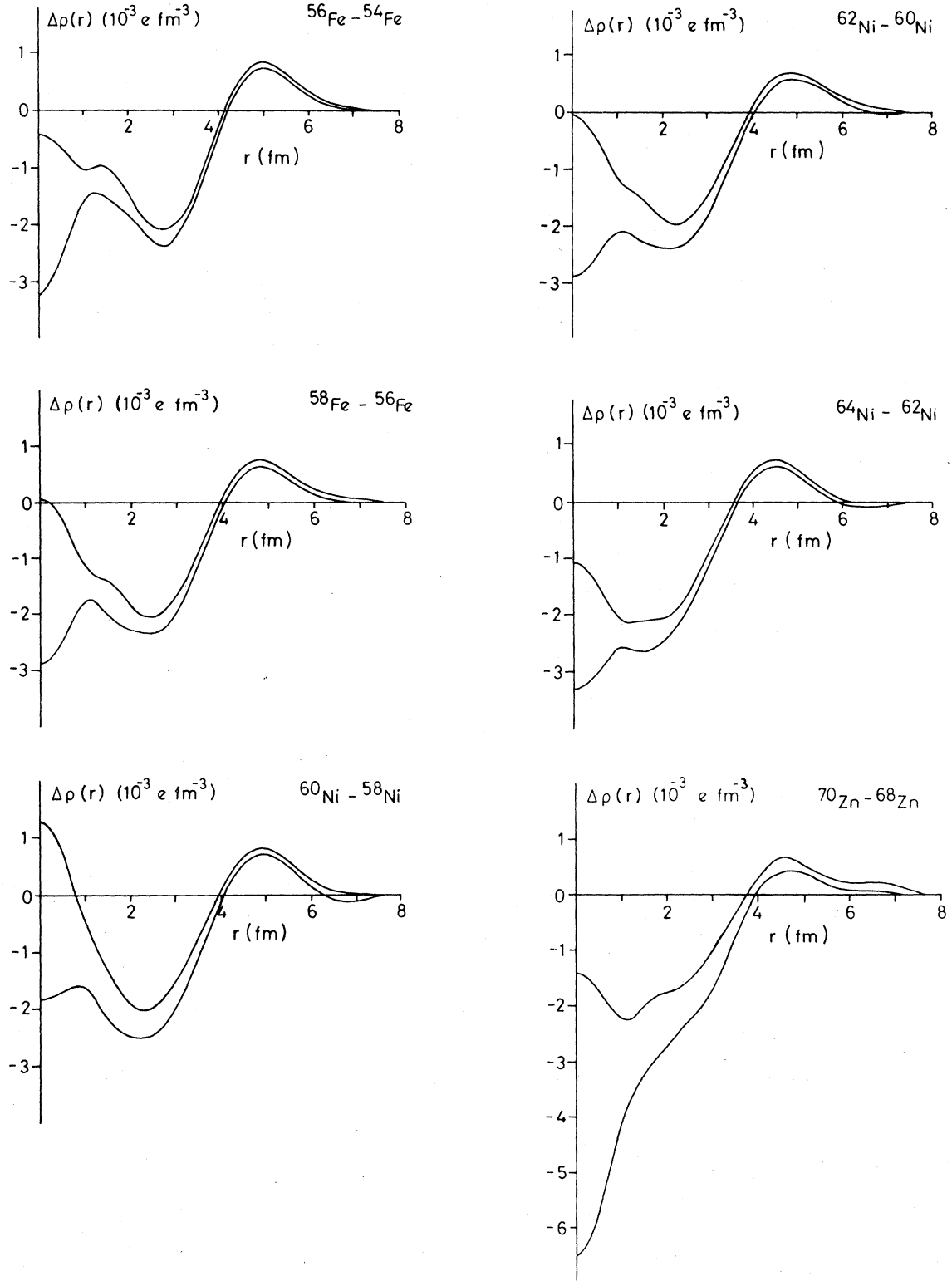

FIG. 4. Charge distribution differences for $\Delta A = 2$ isotope and isotone pairs obtained with the Fourier-Bessel method. The continuous lines are the upper and lower limits of the charge distribution differences deduced from the combined analysis of the elastic electron scattering data and the muonic x-ray data.

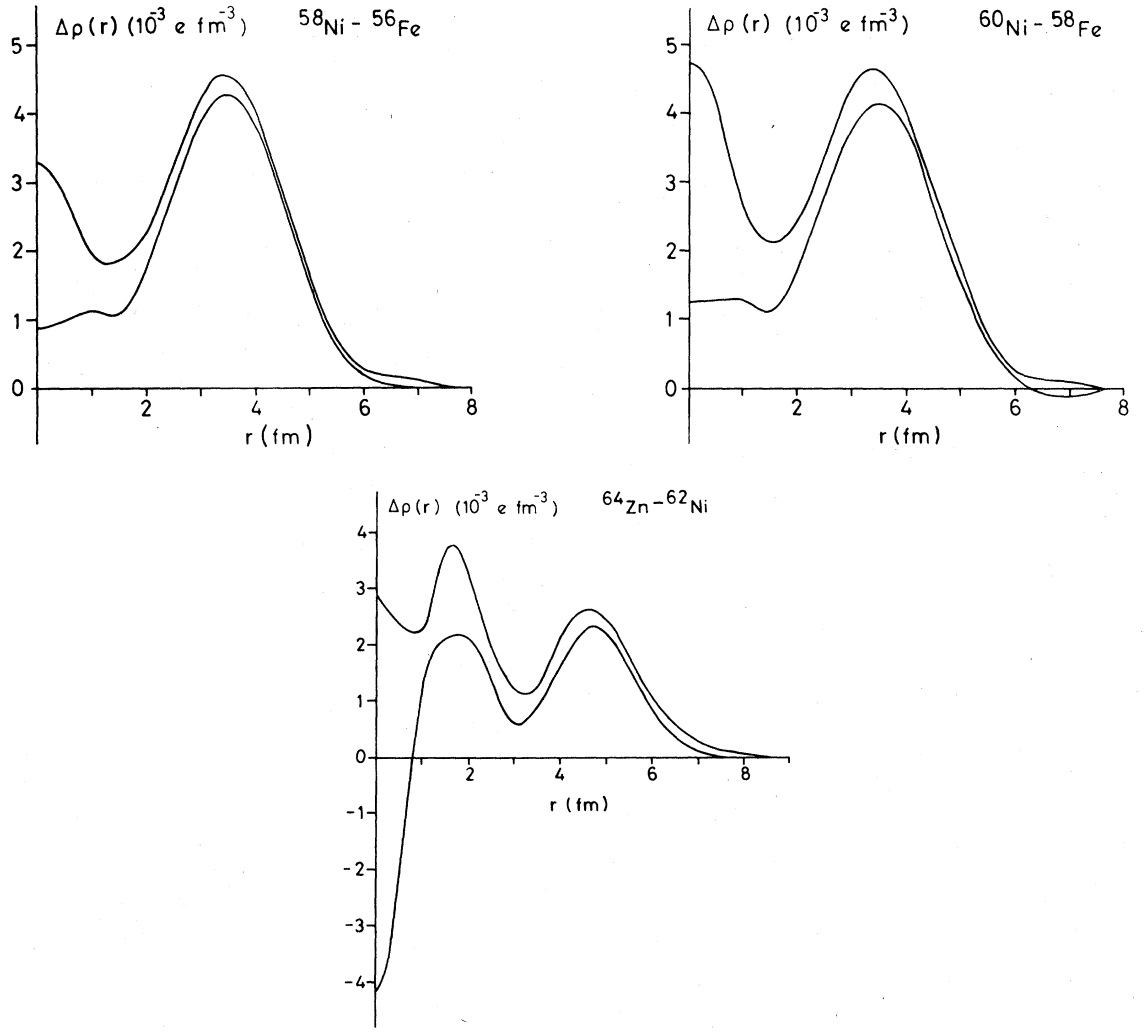

FIG. 4. (*Continued*).

decreased to half of the average density of the central 2 fm region, and the corresponding surface width t_{FB}, defined by the value of Δr for which the charge distribution decreases from 90% to 10% of the 2 fm averaged "central charge density." The results of this analysis are displayed in Fig. 9, which shows that—independent of the neutron number—the half "central charge density" radius *increases* by about $\Delta c = 33 \times 10^{-3}$ fm for each added neutron pair. The corresponding change of the surface width *decreases* nearly linearly as a function of the neutron number. At the beginning of the $2p_{3/2}$ neutron shell (^{56}Fe-^{54}Fe) we observe a large *increase* of the surface width; in the $1f_{5/2}$ neutron shell (^{64}Ni-^{62}Ni), (^{68}Zn-^{66}Zn) and in the $2p_{1/2}$ neutron shell (^{70}Zn-^{68}Zn) the surface width *decreases* with added neutron pairs. An interpretation of this result is given in Sec. IV.

The charge distribution difference for isotone pairs depends predominantly on the charge distribution of the added protons, modified by additional core polarization effects. In Fig. 4 the shell closure effect for $Z = 28$ can therefore clearly be observed: the charge distribution differences for ^{58}Ni-^{56}Fe and ^{60}Ni-^{58}Fe exhibit the characteristic $1f_{7/2}$ proton distribution while the ^{64}Zn-^{62}Ni difference exhibits the $2p_{3/2}$ proton distribution.

The Fourier-Bessel coefficients a_ν, which were fitted to the absolute cross section of ^{60}Ni, are listed in Table III. Since the cross sections were not only measured for the characteristic momentum transfers $q_\nu = \nu\pi/R_{max}$, some coefficients a_ν, corresponding to q_ν beyond the measured momentum transfer range of 2.3 fm^{-1} could be determined due to the inherent correlation properties of the

TABLE III. Fourier-Bessel amplitudes a_ν for the ^{60}Ni reference nucleus. A cutoff radius $R_{max} = 9$ fm was used.

ν	a_ν (fm^{-3}) $\times 10^{()}$
1	2.0082 ± 0.0010 (–2)
2	2.8271 ± 0.0035 (–2)
3	–2.2381 ± 0.0422 (–3)
4	–1.5398 ± 0.0039 (–2)
5	–1.9776 ± 0.0378 (–3)
6	5.7499 ± 0.0670 (–3)
7	2.1057 ± 0.3710 (–3)
8	–0.3787 ± 1.0761 (–3)
9	1.6575 ± 8.2757 (–4)
10	–0.6734 ± 5.6723 (–4)
11	0.2678 ± 3.7350 (–4)
12	–0.1042 ± 2.3825 (–4)
13	0.0395 ± 1.4831 (–4)
14	–0.1450 ± 9.0500 (–5)
15	0.0516 ± 5.4194 (–5)
16	–0.0178 ± 3.1860 (–5)
17	0.0059 ± 1.8382 (–5)

Fourier-Bessel method.[10]

Figure 5 displays the resulting charge distribution for ^{60}Ni and its error band, which includes also the systematic errors of the measurement. The lower section of Fig. 5 shows the contributions of the various error types, adding up to the total error band. Such a plot is useful to establish or to verify the proper experimental conditions: the main contribution to the total error band should stem from the model-dependent error $\delta\rho(r)_{MOD}$, which reflects the uncertainty of the cross sections beyond the accelerator limited momentum transfer range within the upper bound specified by Eq. (3). The curve for $\delta\rho(r)_{STA}$ reflects the influence of the statistical errors of our measurement. In order to obtain a realistic error band due to systematic errors $\delta\rho(r)_{SYS}$, an analysis was performed with experimental data which had been changed in the scattering energy by 0.1%, in scattering angle by 0.04 degree, and in absolute cross sections by 1%. The changes were made in such a way as to maximize the effect on the derived charge distribution.

Charge distributions derived with the Fourier-Bessel parametrization of the charge distribution are listed in Table IV. The quoted errors include both the statistical and model error. The systematic errors, which are the same for all $\rho(r)$, can be obtained from Fig. 5.

III. COMBINED ANALYSIS OF ELASTIC ELECTRON SCATTERING AND MUONIC ATOM TRANSTIONS

The derivation of a nuclear charge distribution by means of a combined analysis of electron scattering and muonic atom x-ray data can most conveniently be performed if the muonic atom transition energies are used to specify a model-independent quantity of the nuclear charge distribution, which can then be used as a constraint while fitting the electron scattering data. In this way the extensive computation procedure required to fit the charge distribution parameters simultaneously to both the scattering cross sections (with a phase shift analysis) and to the muonic atom transition energies (by solving the Dirac equation) can be avoided. This method is only applicable, however, if the residual model dependence of the selected "model-independent" quantity is small compared to the experimental error of the muonic data.

Since the potential $V_\mu(r)$, generated by the bound muon, turns out to be quite insensitive to changes of the nuclear charge distribution, the energy

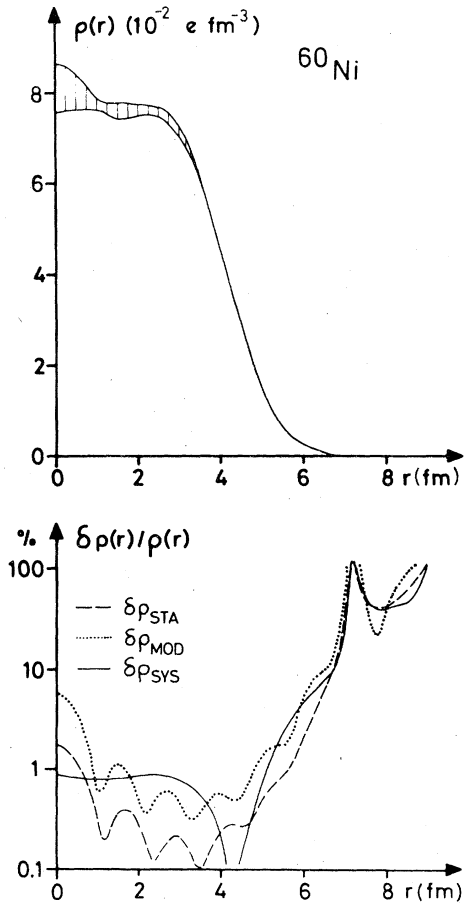

FIG. 5. Fourier-Bessel deduced charge distribution of ^{60}Ni. The error band includes the statistical error of the cross sections, the model error due to the unmeasured momentum transfer range, and systematic uncertainties.

shift of a muonic transition between the levels i and f due to changes $\Delta\rho(r)$ of a spherical nuclear charge distribution is, in first order approximation, given by

$$\Delta E = 4\pi \int_0^\infty \Delta\rho(r)[V_\mu^i(r) - V_\mu^f(r)]r^2 dr, \quad (4)$$

which indicates that $\int \rho(r)[V_\mu^i(r) - V_\mu^f(r)]r^2 dr$ is the desired model-independent quantity.

It has been shown by Barrett[11] that in the region of overlap with the nuclear charge distribution the potential difference can be approximated with good accuracy by

$$V_\mu^i(r) - V_\mu^f(r) = A + Br^k e^{-\alpha r} \quad (5)$$

so that the "Barrett moment"

$$\langle r^k e^{-\alpha r}\rangle = (4\pi/Ze)\int_0^\infty \rho(r) r^k e^{-\alpha r} r^2 dr \quad (6)$$

can be determined model-independently from mu-

TABLE IV. Charge distributions for the investigated nuclei deduced with the Fourier-Bessel parametrization of the charge distribution ($R_{max} = 9$ fm). The quoted errors contain both the statistical errors of the experiment and the model errors associated with the unmeasured higher Fourier-Bessel amplitudes.

r (fm)	$\rho(r)$ (10^{-2} $e$fm^{-3})		
	^{54}Fe	^{56}Fe	^{58}Fe
0.0	8.09(47)	7.79(41)	7.92(39)
0.5	7.98(31)	7.73(27)	7.79(27)
1.0	7.78(6)	7.64(5)	7.54(5)
1.5	7.70(9)	7.59(8)	7.39(7)
2.0	7.75(5)	7.60(4)	7.37(4)
2.5	7.67(4)	7.44(4)	7.26(4)
3.0	7.10(4)	6.87(3)	6.73(3)
3.5	5.84(2)	5.70(2)	5.60(2)
4.0	4.14(3)	4.12(3)	4.09(3)
4.5	2.47(2)	2.52(2)	2.57(2)
5.0	1.21(2)	1.27(2)	1.36(2)
5.5	0.507(13)	0.564(12)	0.613(12)
6.0	0.189(13)	0.225(12)	0.231(11)
6.5	0.073(10)	0.085(8)	0.088(9)
7.0	0.022(8)	0.020(7)	0.033(7)
7.5	0.0022(54)	0.0036(48)	0.0071(48)
8.0	−0.0017(46)	0.0032(43)	−0.0031(42)
8.5	−0.0004(17)	0.0011(15)	−0.0012(15)

	^{58}Ni	^{60}Ni	^{62}Ni	^{64}Ni
0.0	8.07(47)	8.09(44)	7.86(43)	7.66(44)
0.5	7.99(31)	7.98(30)	7.76(28)	7.55(29)
1.0	7.82(6)	7.75(6)	7.56(5)	7.33(6)
1.5	7.76(9)	7.61(8)	7.42(8)	7.18(8)
2.0	7.81(5)	7.63(5)	7.41(4)	7.17(5)
2.5	7.77(4)	7.58(2)	7.35(4)	7.17(4)
3.0	7.29(4)	7.14(4)	6.96(4)	6.86(4)
3.5	6.14(3)	6.05(2)	5.97(2)	5.96(2)
4.0	4.51(3)	4.51(3)	4.51(3)	4.55(3)
4.5	2.80(2)	2.86(2)	2.91(2)	2.97(2)
5.0	1.44(2)	1.52(2)	1.57(2)	1.62(2)
5.5	0.633(13)	0.682(13)	0.729(11)	0.752(13)
6.0	0.247(13)	0.261(12)	0.290(12)	0.292(12)
6.5	0.094(10)	0.097(9)	0.106(9)	0.099(9)
7.0	0.027(8)	0.028(8)	0.026(8)	0.022(8)
7.5	0.0035(55)	−0.0020(51)	0.0004(49)	0.0035(50)
8.0	−0.0003(48)	−0.0071(44)	−0.0023(44)	0.0026(43)
8.5	0.0001(18)	−0.0018(16)	−0.0004(16)	0.0009(13)

TABLE IV. (*Continued.*)

r (fm)	$\rho(r)$ (10^{-2} $e$fm^{-3})			
	^{64}Zn	^{66}Zn	^{68}Zn	^{70}Zn
0.0	7.82(34)	7.93(34)	7.95(33)	7.77(37)
0.5	7.79(23)	7.85(23)	7.80(22)	7.59(26)
1.0	7.73(5)	7.71(5)	7.50(5)	7.24(7)
1.5	7.69(6)	7.61(6)	7.28(6)	6.99(7)
2.0	7.67(4)	7.57(4)	7.23(4)	6.98(5)
2.5	7.52(3)	7.45(3)	7.20(3)	7.02(3)
3.0	7.06(3)	7.01(3)	6.88(3)	6.78(4)
3.5	6.08(2)	6.05(2)	6.02(2)	5.97(2)
4.0	4.69(2)	4.69(2)	4.70(2)	4.69(2)
4.5	3.15(1)	3.17(1)	3.22(1)	3.23(2)
5.0	1.81(1)	1.84(1)	1.90(1)	1.94(1)
5.5	0.900(11)	0.919(11)	0.975(10)	1.01(1)
6.0	0.388(9)	0.382(9)	0.410(9)	0.426(10)
6.5	0.155(8)	0.142(8)	0.140(7)	0.141(9)
7.0	0.0503(63)	0.0484(63)	0.0392(62)	0.0435(79)
7.5	0.0127(42)	0.0212(41)	0.0219(40)	0.0352(45)
8.0	0.0024(39)	0.0093(39)	0.0147(37)	0.0255(47)
8.5	0.0004(13)	0.0018(13)	0.0034(12)	0.0057(15)

onic atom transition energies. The parameter k, which varies slowly with Z and depends on the particular muonic transition and the parameter α, depending linearly on Z, have both been determined by Engfer *et al.*[6]

The Barrett moment can be used to define the equivalent nuclear charge radius R_k of a homogeneously charged sphere by means of the relationship

$$(3/R_k^3)\int_0^{R_k} r^k e^{-\alpha r} r^2 dr = \langle r^k e^{-\alpha r}\rangle . \qquad (7)$$

The Barrett moments and their corresponding equivalent radii R_k which have been used for our combined analysis are listed in the second and third columns of Table V. The quoted errors for these quantities do include the uncertainty of the nuclear polarization correction, which amounts to 0.02 fm^k for the Barrett moments and 0.0045 fm for the equivalent radii, respectively. Further information about the muonic data may be obtained from Ref. 8.

The model independence of the Barrett moments was quantitatively checked by using two different

TABLE V. Radial moments $M(k)$ deduced from a combined analysis of elastic electron scattering data and muonic x-ray data with the Fourier-Bessel parametrization of the charge distribution. In columns 2 and 3 the Barrett moments and equivalent radii deduced from the muonic x-ray experiment (Ref. 8) are listed.

	Muonic x ray		Electron scattering + muonic x ray $M(k)$			
Nucleus	$\langle r^k e^{-\alpha r}\rangle$ (fm^k)	R_k (fm)	$k=1$ (fm)	$k=2$ (fm)	$k=3$ (fm)	$k=4$ (fm)
^{54}Fe	11.856(24)	4.739(5)	3.509(3)	3.694(5)	3.857(9)	4.004(16)
^{56}Fe	12.111(24)	4.794(5)	3.549(3)	3.739(5)	3.905(9)	4.056(16)
^{59}Fe	12.336(25)	4.843(5)	3.584(3)	3.777(5)	3.945(9)	4.097(16)
^{58}Ni	12.272(23)	4.843(5)	3.588(3)	3.777(5)	3.944(11)	4.095(18)
^{60}Ni	12.490(23)	4.890(5)	3.625(3)	3.815(6)	3.983(12)	4.135(24)
^{62}Ni	12.665(23)	4.928(5)	3.659(3)	3.844(5)	4.010(11)	4.161(19)
^{64}Ni	12.779(23)	4.952(5)	3.673(3)	3.862(5)	4.027(11)	4.175(19)
^{64}Zn	13.141(24)	5.037(5)	3.731(3)	3.932(5)	4.109(11)	4.268(20)
^{66}Zn	13.268(24)	5.064(5)	3.751(3)	3.955(6)		
^{68}Zn	13.371(24)	5.086(5)	3.770(3)	3.970(5)	4.145(11)	4.304(20)
^{70}Zn	13.481(27)	5.109(6)	3.787(3)	3.986(5)	4.160(11)	4.318(16)

and very general parametrizations of the nuclear charge distribution. Charge distributions, parametrized as a sum of δ functions (a method first used by Lenz[29]) were simultaneously fitted by Sepp[30] to electron scattering data and the muonic transition data of a CERN-Mainz collaboration[31] for ^{56}Fe. The Barrett moments, derived from all charge distributions which fitted the data, varied within a range corresponding to an uncertainty of the muonic transition energy of 15 eV. A similar result was independently obtained by using a Fourier-Bessel parametrization of the nuclear charge distribution. Since the x-ray transition energies have an experimental error of about 50 eV, the method discussed above for the combined analysis is justified. After Fourier-Bessel parametrized charge distributions were fitted to the electron scattering data, using the Barrett moments as a constraint, these parametrized charge distributions were used to derive radial moments $M(k)$, defined by

$$M(k)=\begin{cases}\left[(4\pi/Ze)\int_0^\infty \rho(r)r^{k+2}dr\right]^{1/k}, & k\neq 0\\ \exp\left[(4\pi/Ze)\int_0^\infty \rho(r)\ln r^2 dr\right], & k=0.\end{cases} \tag{8}$$

In a manner similar to that already outlined for the charge distribution error analysis, the errors of the radial moments $M(k)$ can be analyzed in terms of statistical errors, model-dependent errors, and systematic errors by using the methods discussed in Ref. 10.

The advantage of a combined analysis of muonic atom and electron scattering data can be qualitatively understood by recalling that the experimental information about the nuclear charge density for both experiments can be expressed by integral quantities of the form

$$\int_0^\infty \rho(r)w(r)r^2\,dr. \tag{9}$$

The charge distribution sensitive part of the weighting function $w(r)$ for electron scattering experiments depends on the momentum transfer q and is, in first order Born approximation, given by

$$w_{(e,e)}(r)=j_0(qr)-1, \tag{10}$$

whereas the muonic transition energy information is associated with the weighting function

$$w_\mu(r)=r^k e^{-\alpha r}. \tag{11}$$

Figure 6 shows plots of various weighting functions together with the nuclear charge distribution $r^2\rho(r)$, which demonstrate that the experimental

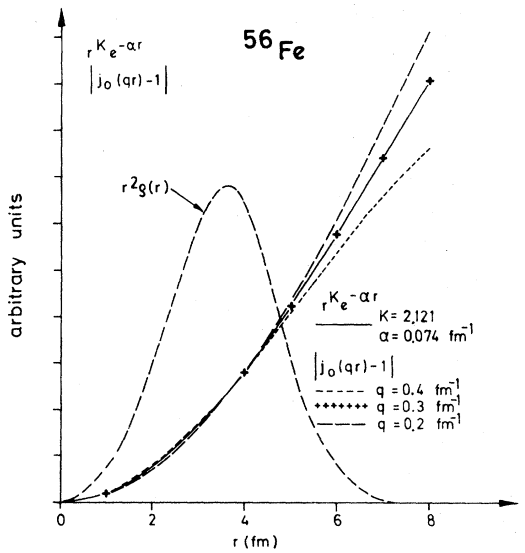

FIG. 6. Comparison of the charge distribution weighting function of the elastic electron scattering $j_0(qr)-1$ with the weighting function $r^k e^{-\alpha r}$ of the muonic $2p_{3/2}$-$1s_{1/2}$ transition. The two weighting functions are adjusted to each other in the maximum of $r^2\rho(r)$ at $r=3.65$ fm.

information of the muonic $2p_{3/2}$-$1s_{1/2}$ transition energy is (for the nuclei near Fe) equivalent to an electron scattering experiment with a momentum transfer of $q\simeq 0.3$ fm^{-1} (see also Ref. 32). The muonic transition energy determines the first parameter a_1 of the Fourier-Bessel parametrization of the nuclear charge distribution with an accuracy which cannot presently be achieved with electron scattering experiments.

For properly devised electron scattering experiments the nuclear charge distribution error band should be determined predominantly by the contribution of the model-dependent error. In that case the accuracy of the charge distribution is limited solely by the high Fourier-Bessel amplitudes a_ν that are not measured in the electron scattering experiment. Therefore, a combined analysis will only insignificantly improve the charge distribution error band. If in an electron scattering experiment the contribution to the error band due to the normalization uncertainty is not negligible (see Fig. 5), this error can substantially be reduced by using the precisely known muonic Barrett moment to determine the normalization.

The influence of the muonic data on the accuracy of the radial moments is, however, profoundly different. The main contribution to the error of the low Fourier-Bessel amplitudes are the normalization uncertainties of the cross sections. The unmeasured high Fourier-Bessel components contribute only insignificantly to the radial moments

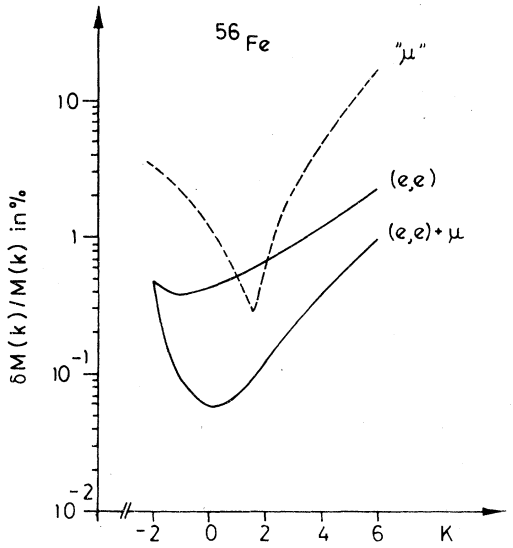

FIG. 7. Relative errors $\delta M(k)/M(k)$ of the radial moments $M(k)$ of the charge distribution from the Fourier-Bessel analysis of the electron scattering data (e,e) and from the combined analysis with the muonic x-ray data $(e,e)+\mu$ for ^{56}Fe. The dashed curve μ shows the information about the radial moments, which can be deduced from muonic x-ray data alone. For details, see text.

whose errors are predominatly determined by the accuracy of the low Fourier-Bessel amplitudes.[10] Using the muonic data to normalize the cross sections, the high precision of the muonic data can substantially reduce the errors of the radial moments in a combined analysis.

The general effect of a combined analysis is quantitatively demonstrated by the curves of Fig. 7, which display the errors for the radial moments $M(k)$, resulting from an electron scattering data analysis [solid curve (e,e)] and a combined analysis [solid curve $(e,e)+\mu$] respectively. The plots depict the total error, originating in the following error sources.

(1) Statistical and model-dependent errors of the Fourier-Bessel analysis.

(2) Errors introduced by the choice of the charge distribution cutoff radius R_{max}. To estimate this error, analyses with different ($8 \leq R_{max} \leq 10$ fm) cutoff radii have been performed. The illustrated errors correspond to the changes of the deduced radial moments.

(3) Systematic errors of the electron scattering data, taking into account the uncertainties of the absolute cross section, the scattering energy, and the scattering angle.

(4) Systematic errors due to the uncertainty of the theoretical corrections for the muonic atom data.

The accuracy of the radial moments, derived from electron scattering data alone, is limited by the systematic errors for radial moments up to $k=4$. The error for a combined analysis for the radial moment range $-1 \leq k \leq 4$ originates predominantly from the uncertainty of the nuclear polarization correction for the muonic atom transition energies.

In order to demonstrate the influence of the electron scattering data on the accuracy of the radial moments, an analysis has been performed in which the influence of the electron scattering data was considerably reduced by assuming an electron scattering cross section error of 100%. The results of this analysis are shown by the dashed curve labeled "μ" in Fig. 7. This plot demonstrates that the accuracy for the rms radius will be improved by a factor of 5 if the electron scattering information is included. This indicates that for extrapolating the precisely known Barrett moment to values for the rms radius, and other radial moments, the knowledge about the charge distribution by means of electron scattering data is essential. The "μ" curve shows further that the radial moment for $k=1.5$ is the moment $M(k)$ most precisely determined by muonic data. The relative error for this moment is, however, still a factor of 3 larger than the experimental error of the Barrett moment. The radial moments $M(k)$ for $k=1$ to 4, resulting from the combined analysis of electron scattering and muonic atom data, are listed in Table V. The quoted errors are total errors and also include the uncertainty due to the model dependence. The main contribution to these errors originates from an assumed 40% uncertainty in the nuclear polarization correction.[8]

The main contribution to the total error of the rms radius obtained from a combined analysis results from the uncertainty of the nuclear polarization correction. Since the nuclear polarization correction is expected to vary slowly with the mass number, differences between radial moments for various isotopes and isotones have a higher accuracy than the absolute values. The differences of rms radii, presented in Table VI and Fig. 8, have been derived from a combined analysis of the measured cross section ratios and the measured muonic isotope and isotone shifts. The Barrett moment differences were used as an additional experimental point in the adjustment of the Fourier-Bessel parametrized charge distribution differences. The quoted errors include the different contributions discussed above, with the exception of the nuclear polarization correction, since this uncertainty cancels to a large extent.

The comparison of the rms radii resulting from the electron scattering data analysis with those

TABLE VI. Rms radii differences $\Delta\langle r^2\rangle^{1/2}$ and differences of $\langle r^4\rangle^{1/4}$ deduced from the combined analysis of the elastic electron scattering cross section ratios and the muonic isotope and isotone shifts (Ref. 8). The results of this work are compared with previous results of elastic electron scattering compiled in Ref. 5.

Nuclei pair	$\Delta\langle r^2\rangle^{1/2}$ (10^{-3} fm) $(e,e)+\mu$ this work	(e,e) comparison		$\Delta\langle r^4\rangle^{1/4}$ (10^{-3} fm) $(e,e)+\mu$ this work
^{56}Fe-^{54}Fe	44.5 ± 0.8	69 ± 14 (Ref. 33)		51.8 ± 4.3
^{58}Fe-^{56}Fe	38.2 ± 1.0	4 ± 18 (Ref. 33)		41.3 ± 5.1
^{60}Ni-^{58}Ni	37.3 ± 1.1	51 ± 14 (Ref. 34)	32 ± 14 (Ref. 35)	43.8 ± 8.7
^{62}Ni-^{60}Ni	28.6 ± 0.8		26 ± 14 (Ref. 35)	22.8 ± 7.1
^{64}Ni-^{62}Ni	18.1 ± 0.6		23 ± 14 (Ref. 35)	13.5 ± 4.5
^{66}Zn-^{64}Zn	22.5 ± 3.0	25 ± 13 (Ref. 34)	39 ± 7 (Ref. 36)	
^{68}Zn-^{66}Zn	14.4 ± 3.0		−16 ± 9 (Ref. 36)	
^{70}Zn-^{68}Zn	17.3 ± 2.5		47 ± 15 (Ref. 36)	10.6 ± 9.9
^{58}Ni-^{56}Fe	38.6 ± 1.0	−22 ± 13 (Ref. 34)		39.7 ± 4.9
^{60}Ni-^{58}Fe	38.2 ± 2.3			44.7 ± 10.0
^{64}Zn-^{62}Ni	89.3 ± 1.2			108.3 ± 8.0
^{66}Zn-^{64}Ni	93.8 ± 5.0			

derived from the combined analysis, which are mainly determined by the muonic atom experiment, averaged over all investigated nuclei, gives the following result: $\langle r^2\rangle_{(e,e)}^{1/2} - \langle r^2\rangle_{(e,e)+\mu}^{1/2} = (-11 \pm 26)\times 10^{-3}$ fm. It should, however, be mentioned that this quoted difference results from using electron scattering data that are not dispersion corrected. Omitting the nuclear polarization effects also for the muonic atom data,[37] the difference reduces to -2×10^{-3} fm. By including dispersion corrections to the electron scattering data, as calculated by Rosenfelder,[38] the difference will be increased to -20×10^{-3} fm. At present the large error, which is mainly caused by the systematic errors of the electron scattering data, prevents any decisive conclusion about the internal consistency of the two different experimental methods. It is, however, planned to investigate this problem more thoroughly at Mainz by a precise measurement of the absolute ^{60}Ni electron scattering cross section.

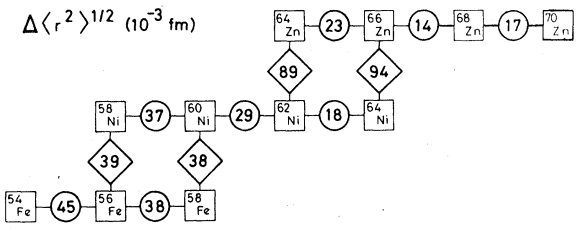

FIG. 8. Differences of the rms radii for adjacent nuclei in units of 10^{-3} fm. The errors of the model-independent differences are a few 10^{-3} fm (see Table VI).

IV. INTERPRETATION AND CONCLUSIONS

Our results for charge distribution differences of isotope pairs in the region $28 \leq N \leq 40$, differing by two neutrons, are compiled in Fig. 9. All isotope pairs exhibit the following general trends.

(a) The changes $\Delta\langle r^2\rangle^{1/2}$ of the rms radii decrease nearly linearly with increasing neutron number.[8] Thus it is possible to describe the absolute rms radii of these even-even nuclei by a polynomial of second order in the neutron number:

$$\langle r^2\rangle^{1/2} = r_0 + a(N-28) + b(N-28)^2 + \delta_{\pm}(Z-28)$$

where $26 \leq Z \leq 30$, $28 \leq N \leq 38$, $r_0 = 3.734$ fm, $a = 2.398\times 10^{-2}$ fm, $b = -9.655\times 10^{-4}$ fm, $\delta_+ = 4.575\times 10^{-2}$ fm, $\delta_- = 1.925\times 10^{-2}$ fm. (This formula reproduces the measured absolute rms radii within a deviation of 2×10^{-3} fm.) The proton shell closure at $Z = 28$ is taken into account by $\delta_{\pm}$, where the index refers to the sign of the difference $(Z-28)$. The dashed lines in Figs. 9 and 12 refer to the derivative of this equation. The departure of the ^{70}Zn-^{68}Zn point from the formula seems to indicate a subshell at $N = 38$.

(b) Within the experimental error, the changes Δc_{FB} of the half "central charge density" (average of the central 2 fm region) radius are constant and given by $\Delta c_{FB} = (33 \pm 10)\times 10^{-3}$ fm.

(c) The change Δt_{FB} of the surface thickness decreases nearly linearly with increasing neutron number and changes sign while the $2p_{3/2}$, $1f_{5/2}$, and $2p_{1/2}$ neutron shells are being filled: At the beginning of these shells (^{56}Fe-^{54}Fe) the surface thickness increases strongly; the surface thick-

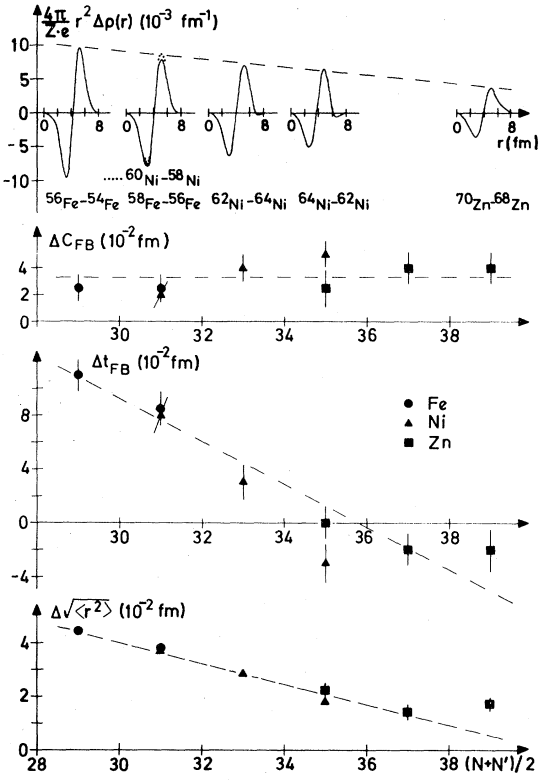

FIG. 9. Charge distribution differences $(4\pi/Ze)r^2\Delta\rho(r)$, changes of the half density radius Δc_{FB}, and the skin thickness Δt_{FB} and rms radii differences $\Delta\langle r^2\rangle^{1/2}$ for the $\Delta N = N' - N = 2$ isotope shifts. The dashed lines emphasize the observed systematics. The results for ^{58}Fe-^{56}Fe and ^{60}Ni-^{58}Ni indicate the independence of the charge distribution differences from the proton configuration.

ness decreases, however, while adding the last four neutrons of these shells. The changes of the surface thickness are also reflected by the ratios $\Delta M(4)/\Delta M(2)$, which can be deduced from Table VI.

(d) The amplitude of the rearrangement effect, depicted by $(4\pi/Ze)r^2\Delta\rho(r)$, decreases linearly with increasing neutron number, while the zero crossing of $(4\pi/Ze)r^2\Delta\rho(r)$ shifts slightly to smaller radii (for details see Fig. 4).

(e) The above effects tend to be independent of the proton number as can be seen by comparing the data of Fig. 9 for ^{60}Ni-^{58}Ni and ^{58}Fe-^{56}Fe. The independence of the isotope shifts upon the proton configuration was first observed for the neodymium and samarium isotopes by Brix and Kopfermann.[39]

In the following we try to extract from the measured isotone charge distribution differences, the rearrangement effect of the proton core due to the added protons and compare it with the rearrangement effect of the proton core due to the added neutrons. The latter is given directly by the measured isotope charge distribution differences. To separate the rearrangement contribution from the measured isotone charge distribution differences, we substract the spatial distribution of the added protons, using harmonic oscillator wave functions [see Figs. 11(b) and 11(c)] with an oscillator parameter[40]

$$b^2 = 41.11/(45A^{-1/3} - 25A^{-2/3})\ \text{fm}^2,$$

and interpret the result as rearrangement effect. The resulting core rearrangements for ^{58}Ni-^{56}Fe and ^{64}Zn-^{62}Ni are shown in Figs. 10(a) and 10(b). These figures depict also the corresponding core rearrangement due to added neutrons for the ^{50,48}Ti (Refs. 41, 42) and ^{56,54}Fe pairs. Closing the $1f_{7/2}$ proton shell (^{58}Ni-^{56}Fe) and the $1f_{7/2}$ neutron shell (^{50}Ti-^{48}Ti), one obtains similar rearrangement effects, which give a negative contribution to the rms radii differences. The first two protons (^{64}Zn-^{62}Ni) and neutrons (^{56}Fe-^{54}Fe) added into the $2p_{3/2}$ shell also show a similar rearrangement effect. However, the contribution of the rearrangement effect to the rms radii difference is positive in this case. This indicates that the core polarization change when crossing the shell closure at

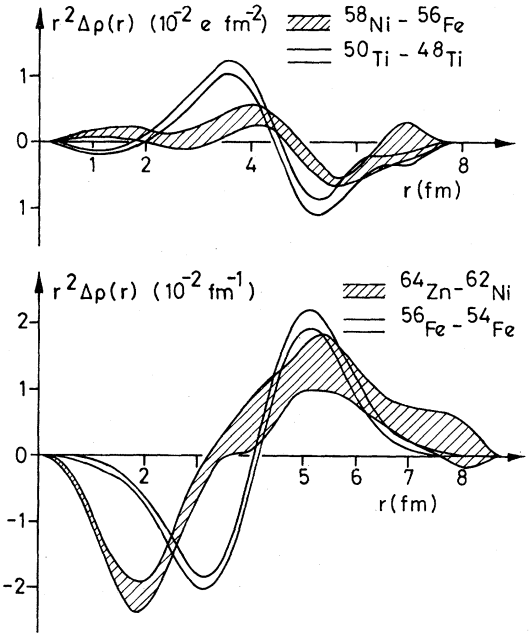

FIG. 10. Comparison of rearrangement effects due to $1f_{7/2}$ and $2p_{3/2}$ protons (^{58}Ni-^{56}Fe, ^{64}Zn-^{62}Ni) with that due to the corresponding neutrons [^{50}Ti-^{48}Ti (Refs. 41, 42), ^{56}Fe-^{54}Fe]. The isotope rearrangement effects are measured directly, whereas the isotone rearrangement effects are extracted from the measured charge distribution differences after subtraction $1f$ or $2p$ harmonic oscillator wave functions, respectively.

$Z = 28$ gives a substantial contribution to the observed change of the isotone shifts which occurs at the closure of the $1f_{7/2}$ and at the start of the $2p_{3/2}$ proton shell, respectively (see Fig. 8). A similar result with a rearrangement effect being positive at the beginning of the $1f_{7/2}$ proton (Ti-Ca) and neutron (^{42}Ca-^{40}Ca) shells has been obtained from a systematic investigation of all $1f_{7/2}$ shell nuclei.[42]

Density dependent deformed Hartree-Fock calculations (DDHF) for the nuclei investigated in this work have been performed by Negele and Rinker.[43] The predictions of these calculations for charge distribution differences and rms radii differences depend strongly upon the deformation of the two nuclei compared. The calculations indicate that the Fe, Ni, and Zn nuclei are very soft in respect to shape deformations; i.e., the total nuclear binding energy does not show a well defined minimum as a function of deformation for most nuclei in this region.

The result of the DDHF calculations for various assumed deformations of ^{54}Fe and ^{56}Fe (Ref. 43) are compared with the experimental ^{56}Fe-^{54}Fe charge distribution difference $r^2\Delta\rho(r)$ in Fig. 11(a). The calculated difference, assuming that both ^{56}Fe and ^{54}Fe are spherical, represented by the solid line, is about a factor of 3 smaller than the experimental result. A prolate deformation calculation for both nuclei underestimates the experimental result, whereas the extreme case of comparing a spherical ^{54}Fe with a prolate deformed ^{56}Fe overestimates the experimentally observed rearrangement of the proton core. This suggests that a superposition of solutions, using various deformations for the two involved nuclei, via the generator coordinate method, will provide better agreement between theory and experiment than the results shown, which are deduced using a single intrinsic state for each of the two nuclei.

Experimentally determined $r^2\Delta\rho(r)$ for the isotone pairs ^{58}Ni-^{56}Fe and ^{64}Zn-^{62}Ni are compared in Figs. 11(b) and 11(c) with the charge distribution differences derived from the harmonic oscillator wave functions of the two added protons and with results of the DDHF calculations.[43] The exaggerated structure of the pure harmonic oscillator wave functions compared to the experimental result indicates again that core rearrangement effects are important. The comparison of the two different DDHF results with the experimental charge distribution difference of ^{64}Zn-^{62}Ni suggests, as outlined above, that a superposition of calculations with various deformations may be appropriate.

The systematic changes of the surface thickness and rms radii, which were illustrated in Fig. 9, suggest that deformation changes occur in the Fe,

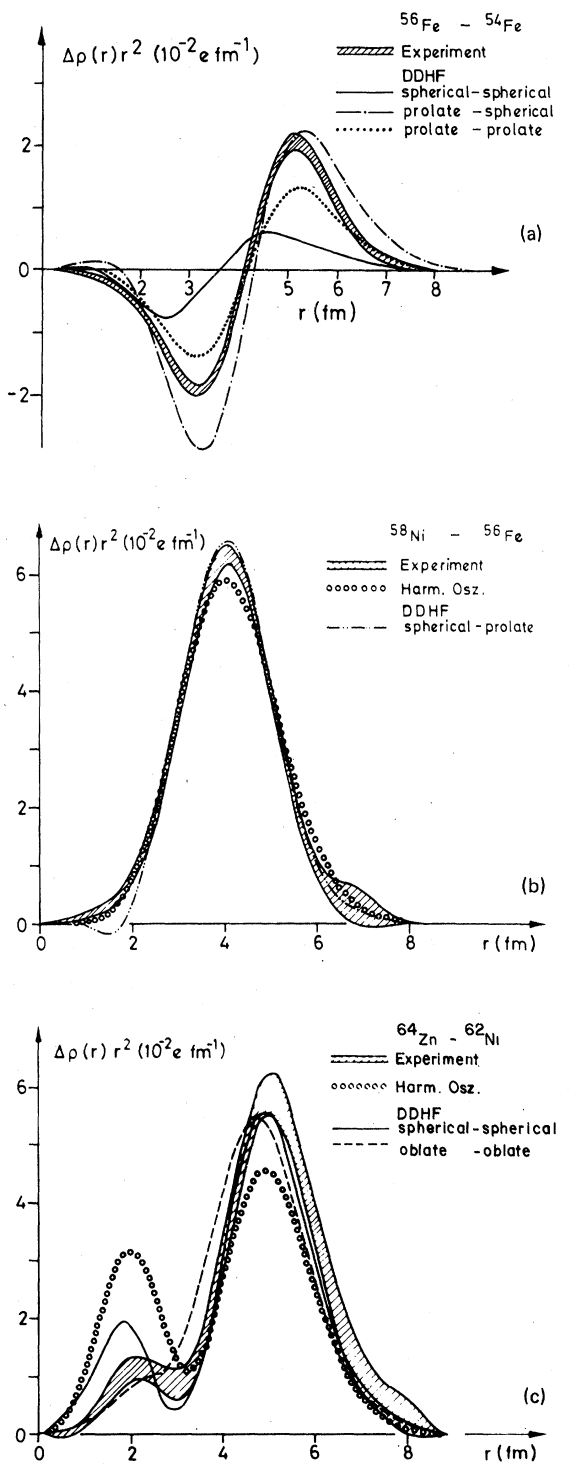

FIG. 11. Comparison of experimental $\Delta A = 2$ isotope (a) and isotone (b), (c) charge distribution differences with density dependent Hartree-Fock (DDHF) calculations by Negele and Rinker (Ref. 43). The calculations shown assume various deformations for both nuclei involved. Shell model calculations with harmonic oscillator wave functions are also shown (open circles).

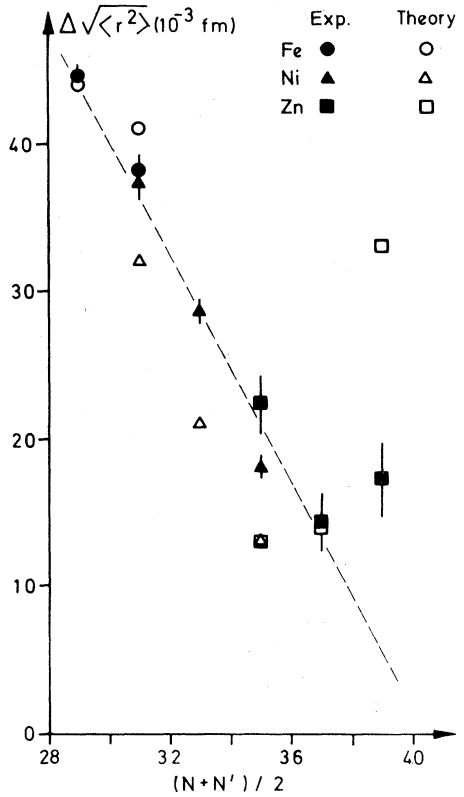

FIG. 12. Comparison of the experimental rms radii differences with the calculations of Reinhard and Drechsel (Ref. 46).

Ni, and Zn nuclei. This idea is supported by the observation that the measured $B(E2)$ values[44] for the first excited collective 2^+ states show the same trend. Phenomenological models,[45] which provide relationships between surface thickness and transition strength, also support this suggestion. Reinhard and Drechsel[46] have recently derived similar relations from a microscopic point of view. In their calculations the bulk properties of the nuclei, varying smoothly and slowly with the nucleon number A, are obtained by spherical Hartree-Fock calculations.[47] In addition, they consider not only the influence of static deformations but also the contribution due to the zero point oscillations of the nuclear excitation modes. These contributions come mainly from the isoscalar 2^+ giant resonance, which varies slowly with the nucleon number A, and from the low lying collective 2^+ state, which shows strong shell structure effects. Both the contribution of the zero point oscillation and the influence of the static deformation are related to experimental $B(E2)$ values. The results of Ref. 46 for the rms radii are compared in Fig. 12 with the experimental values and show a better agreement than the results of deformed DDHF calculations,[43] which do not include the zero point motion.

The accuracy of the experiment and the extraction of the experimental information in a model-independent way allows a clear judgment of the success of various calculations. The comparison of the experimental results with the calculations of Refs. 43 and 46 indicates that deformation effects are important in the charge distribution differences of the investigated nuclei and that ground-state correlations, especially zero point quadrupole (surface) oscillations, seem to contribute substantially to the charge distribution differences of neighboring nuclei.

ACKNOWLEDGMENTS

We are particularily grateful to Prof. Dr. H. Ehrenberg, director of the Institut für Kernphysik, whose unending personal effort made it possible to perform this experiment at the Mainz electron accelerator. We appreciate many fruitful discussions and the helpful cooperation of all our colleagues contributing to this work. Our thanks to the entire laboratory staff for their overall assistance during the measurements. Finally we wish to thank the linac crew for providing the specified electron beam. Also we are thankful to Dr. H. Hintenberger and Mr. H. Jagoutz from the Max-Planck-Institut für Chemie in Mainz for performing analyses of target impurities. This work was supported by the Deutsche Forschungsgemeinschaft and the U. S. Department of Energy.

*Present address: Los Alamos Scientific Laboratory, University of California, Los Alamos, New Mexico 87545.

[1]L. R. B. Elton, *Nuclear Sizes* (Oxford University Press, Belfast, 1961).

[2]H. R. Collard, L. R. B. Elton, and R. Hofstadter, *Landolt-Börnstein Numerical Data and Functional Relationships in Science and Technology*, edited by K.-H. Hellwege (Springer, Berlin, 1967), New Series, Group I, Vol. 2.

[3]P. Brix, Naturwissenschaften 64, 293 (1977).

[4]W. D. Myers, Nucl. Phys. A204, 465 (1973).

[5]C. W. De Jager, H. De Vries, and C. De Vries, At. Data Nucl. Data Tables 14, 479 (1974).

[6]R. Engfer, H. Schneuvly, J. L. Vuilleumier, H. K. Walter, and A. Zehnder, At. Data. Nucl. Data Tables 14, 509 (1974).

[7]K. Heilig and A. Steudel, At. Data Nucl. Data Tables 14, 613 (1974).

[8]E. B. Shera, E. T. Ritter, R. B. Perkins, G. A. Rin-

ker Jr., L. K. Wagner, H. D. Wohlfahrt, G. Fricke, and R. M. Steffen, Phys. Rev. C 14, 731 (1976).
[9]O. Schwentker, thesis, University of Mainz, 1977 (unpublished).
[10]B. Dreher, J. Friedrich, K. Merle, H. Rothhaas, and G. Lührs, Nucl. Phys. A235, 219 (1974).
[11]R. C. Barrett, Phys. Lett. 33B, 388 (1970).
[12]H. Ehrenberg, H. Averdung, B. Dreher, G. Fricke, H. Herminghaus, R. Herr, H. Hultzsch, G. Lührs, K. Merle, R. Neuhausen, G. Nöldecke, H. M. Stolz, V. Walther, and H. D. Wohlfahrt, Nucl. Instrum. Methods 105, 253 (1972).
[13]H. Herminghaus and K. H. Kaiser, Nucl. Instrum. Methods 113, 189 (1973).
[14]G. Stephan, thesis, University of Mainz, 1973 (unpublished).
[15]R. Steiner, K. Merle, and H. G. Andresen, Nucl. Instrum. Methods 127, 11 (1975).
[16]H. M. Stolz, thesis, University of Mainz, 1973 (unpublished).
[17]H. Rothhaas, Diplomarbeit, University of Mainz, 1971 (unpublished).
[18]Oak Ridge National Laboratory, Tennessee.
[19]H. Hintenberger, Max-Planck-Institut für Chemie, Mainz, private communication.
[20]H. Jagoutz, Max-Planck-Institut für Chemie, Mainz, private communication.
[21]K. Chmillon, Diplomarbeit, University of Mainz, 1972 (unpublished).
[22]W. Reuter, K. Merle, G. Elsner, and G. Fricke (unpublished).
[23]L. C. Maximon, Rev. Mod. Phys. 41, 193 (1969).
[24]D. B. Isabelle and G. R. Bishop, Nucl. Phys. 45, 209 (1963).
[25]E. M. Lyman, A. O. Hanson, and M. B. Scott, Phys. Rev. 84, 626 (1951).
[26]I. Sick, Phys. Lett. 44B, 62 (1973).
[27]J. Borysowicz and J. H. Hetherington, Phys. Rev. C 7, 2293 (1973).
[28]J. L. Friar and J. W. Negele, Nucl. Phys. A212, 93 (1973).
[29]F. Lenz, Z. Phys. 222, 491 (1969).
[30]W. D. Sepp, thesis, University of Freiburg, 1974 (unpublished).
[31]G. Backenstoss, T. Böhringer, H. P. Povel, G. Fricke, and H. D. Wohlfahrt (unpublished); T. Böhringer, Travail de Diplom, ETH Zürich, 1971 (unpublished).
[32]R. Engfer, in *Proceedings of the International Conference on Nuclear Physics, Munich, 1973*, edited by J. de Boer and H. J. Mang (North-Holland, Amsterdam, 1973), Vol. 2, p. 438.
[33]A. S. Litvinenko, N. G. Shevchenko, A. Yu. Buki, G. A. Savitskii, V. M. Khvastunov, and R. L. Kondrat'ev, Yad. Fiz. 14, 40 (1971) [Sov. J. Nucl. Phys. 14, 23 (1972)]; A. S. Litvinenko, N. G. Shevchenko, N. G. Afanas'ev, A. Yu. Buki, G. A. Savitskii, V. M. Khvastunov, A. A. Khomich, I. I. Chkalow, and V. P. Likhachev, Yad. Fiz. 15, 1104 (1972) [Sov. J. Nucl. Phys. 15, 611 (1972)].
[34]V. M. Khvastunov, N. G. Afanas'ev, V. D. Afanas'ev, E. V. Bondarenko, I. S. Gul'karov, G. A. Savitskii, and N. G. Shevchenko, Yad. Fiz. 12, 9 (1970) [Sov. J. Nucl. Phys. 12, 5 (1971)].
[35]I. R. Ficenec, W. P. Trower, I. Heisenberg, and I. Sick in: C. W. De Jager, H. De Vries, and C. De Vries, At. Data Nucl. Data Tables 14, 479 (1974).
[36]R. Neuhausen, J. W. Lightbody, S. P. Fivozinsky, and S. Penner, Phys. Rev. C 5, 124 (1972).
[37]G. A. Rinker, Jr. and L. Wilets, Phys. Rev. D 7, 2629 (1973).
[38]R. Rosenfelder, private communication; J. Knoll and R. Rosenfelder, Nucl. Phys. A229, 333 (1974).
[39]P. Brix and H. Kopfermann, Naturwissenschaften 35, 189 (1948).
[40]J. Blomqvist and A. Molinari, Nucl. Phys. A106, 545 (1968).
[41]J. Heisenberg, R. Hofstadter, J. S. McCarthy, R. Herman, B. C. Clark, and D. G. Ravenhall, Phys. Rev. C 6, 381 (1972).
[42]H. D. Wohlfahrt, E. B. Shera, M. V. Hoehn, Y. Yamazaki, and R. M. Steffen (unpublished).
[43]J. W. Negele and G. Rinker Jr., Phys. Rev. C 15, 1499 (1977).
[44]P. H. Stelson and L. Grodzins, Nucl. Data Sheets A1, 21 (1965).
[45]D. Drechsel and W. Scheid, Z. Phys. 179, 556 (1964).
[46]P. G. Reinhard and D. Drechsel, Z. Phys. A290, 85 (1979).
[47]H. Pfeiffer, Diplomarbeit, University of Mainz, 1977 (unpublished).